**Astronomy
&
Astrophysics**

Characterization of the hot Neptune GJ 436 b with *Spitzer* and ground-based observations[⋆]

B.-O. Demory[1,7], M. Gillon[1,2], T. Barman[3], X. Bonfils[4] M. Mayor[1], T. Mazeh[5], D. Queloz[1], S. Udry[1], F. Bouchy[8], X. Delfosse[6], T. Forveille[6], F. Mallmann[7], F. Pepe[1], and C. Perrier[6]

[1] Observatoire de Genève, Université de Genève, 1290 Sauverny, Switzerland
e-mail: brice-olivier.demory@obs.unige.ch
[2] Institut d'Astrophysique et de Géophysique, Université de Liège, 4000 Liège, Belgium
[3] Lowell Observatory, 1400 West Mars Hill Road, Flagstaff, AZ 86001, USA
[4] Observatório Astronómico de Lisboa, Tapada da Ajuda, 1349-018 Lisboa, Portugal
[5] School of Physics and Astronomy, Raymond and Beverly Sackler Faculty of Exact Sciences, Tel Aviv University, Tel Aviv, Israel
[6] Laboratoire d'Astrophysique de Grenoble, Observatoire de Grenoble, UMR5571 de l'Université J.Fourier et du CNRS, BP 53, 38041 Grenoble, France
[7] Observatoire François-Xavier Bagnoud – OFXB, 3961 Saint-Luc, Switzerland
[8] Institut d'Astrophysique de Paris, UMR7095 CNRS, Université Pierre & Marie Curie, 98bis Bd. Arago, 75014 Paris, France

ABSTRACT

We present *Spitzer Space Telescope* infrared photometry of a secondary eclipse of the hot Neptune GJ 436 b. The observations were obtained using the 8-μm band of the InfraRed Array Camera (IRAC). The data spanning the predicted time of secondary eclipse show a clear flux decrement with the expected shape and duration. The observed eclipse depth of 0.58 mmag allows us to estimate a blackbody brightness temperature of $T_\mathrm{p} = 717 \pm 35$ K at 8 μm. We compare this infrared flux measurement to a model of the planetary thermal emission, and show that this model reproduces properly the observed flux decrement. The timing of the secondary eclipse confirms the non-zero orbital eccentricity of the planet, while also increasing its precision ($e = 0.14 \pm 0.01$). Additional new spectroscopic and photometric observations allow us to estimate the rotational period of the star and to assess the potential presence of another planet.

Key words. techniques: photometric – techniques: spectroscopic – eclipses – stars: individual: GJ 436 – planetary systems – infrared: general

1. Introduction

GJ 436 b is one of the few known Neptune-mass extrasolar planets. It was discovered by radial-velocity measurements (Butler et al. 2004) as a planet with a period of 2.6 days and a minimum mass of 21 $M_\oplus$. Follow-up Doppler observations of GJ 436 refined the planetary mass and the orbital parameters, including an eccentricity of 0.16 ± 0.02 (Maness et al. 2007, hereafter M07). Our team (Gillon et al. 2007a, hereafter G07a) discovered the transiting nature of GJ 436 b, enabling us to measure a planetary radius ~4 $R_\oplus$. This discovery and the corresponding measurements of the planetary radius and mass indicated a planet composed mostly of ice, probably surrounded by a small H/He envelope.

Because of the small size of the parent star ($R \sim 0.4\ R_\odot$) and the short orbital period of GJ 436 b, the planet-to-star luminosity ratio in the infrared is comparable to that of many known hot Jupiters, despite the planet's much smaller radius. Furthermore, the M dwarf GJ 436 is rather bright in the infrared ($K \sim 6$). Detection of the thermal emission from this small planet had thus been expected to be within the reach of the *Spitzer Space Telescope*.

Following our transit discovery, we submitted a Discretionary Director Time (DDT) *Spitzer* proposal to better characterize this interesting planet. We applied for photometric observations of the primary transit using the 8-μm band of the InfraRed Array Camera IRAC (Fazio et al. 2004) in order to get a very accurate radius measurement and constrain the bulk composition of the planet. We also applied for photometric observations of the secondary eclipse in the four bands of IRAC (3.6, 4.5, 5.8 and 8 μm), in the 16-μm band of the InfraRed Spectrograph IRS (Houck et al. 2004), and the 24-μm band of the Multiband Imaging Photometer MIPS (Rieke et al. 2004), to assess the atmospheric temperature, albedo, heat distribution efficiency and composition. However, the observations were actually initiated and performed as part of an existing Target of Opportunity (ToO) program (ID 30129, PI J. Harrington), which has a total priority for the observations of transiting planets. The main goal of this ToO is to deliver to the community, without any proprietary period, optimal *Spitzer* observations of transiting planets.

Spitzer observed the transit and the secondary eclipse of GJ 436 in the 8-μm IRAC band on June 29 and 30, respectively. The data of the primary transit were made publicly available on July 13th 2007. Our direct analysis of these data allowed us to determine a very accurate radius for GJ 436 b ($R_\mathrm{p} = 4.2\ R_\oplus$, Gillon et al. 2007b, hereafter G07b) and to confirm the presence of an H/He envelope. *Spitzer* data of the secondary eclipse

were not released to the community until July 17th 2007, due to an oversight that occurred at the *Spitzer* Science Center. This explains why we separated our analysis and present here our results regarding the secondary eclipse data.

A few days before submission of this paper, a Letter reporting primary and secondary eclipses analyses was submitted to ApJ by Deming et al. (2007). The present analysis was conducted independently from their work and the results of both studies appear complementary.

Analyzing the secondary eclipse data, we report here the detection of a secondary eclipse and draw conclusions about the thermal emission of GJ 436 b, and refine its orbital parameters, allowing a better understanding of GJ 436 dynamics by exploring the contingency of a supplementary planet.

In addition, we report here on additional ground-based observations conducted to determine the stellar rotational period. We followed the photometric intensity and the Ca II H+K activity index of GJ 436. Although the photometric data are sparse and cover only 50 days, we find some evidence that the stellar rotational period is of the order of 50 days, which is also consistent with long-term CaII measurements.

Section 2 describes the observations and the reduction procedure. Our analysis of the obtained secondary eclipse time series is described in Sect. 3. In Sect. 4, we analyze the infrared emission from the planet and draw some conclusions about its atmospheric composition. We detail an orbital analysis, encompassing the possibility of a perturbing planet, stellar activity and GJ 436 b orbital parameters refinements in Sect. 5. Our conclusions are presented in Sect. 6.

2. Observations and data reduction

2.1. Spitzer IRAC observations

GJ 436 has been observed on June 30th UT for 6 h, to cover the secondary eclipse, resulting in 49 920 frames. Observations were made so as to encompass the expected secondary eclipse window; timing calculations were made by taking into account transit timing and orbital eccentricity. Due to the uncertainties on eccentricity and argument of periastron, a larger time-window was chosen to ensure the detection of the secondary eclipse. Data acquisition was made using IRAC in its 8-μm band with the same mode and strategy employed for the primary transit (G07b).

We combine each set of 64 images using a 3-σ clipping to eliminate transient events in the pixel grid, yielding 780 stacked images for the secondary eclipse, with a temporal sampling of ~28 s. Heliocentric Julian Day (HJD) conversion was made according to the mean *Spitzer* orbital position at the time of each exposure and GJ 436's apparent position. *Spitzer* position ephemerides were obtained through JPL-Horizons web interface (Giorgini et al. 1996) and converted from terrestrial dynamic time (TDT) to UTC.

We faced the same instrumental rise issue that was noticed in our work on primary transit. To mitigate its effect, we zero-weight the eclipse and the first 100 points of the time-series. We then divide the lightcurve by the best fitting asymptotic function with three free parameters, and evaluate the average flux outside the eclipse to normalize the time series, exactly as for the primary transit. The rms of the resulting time series evaluated outside the eclipse is the same as for the primary (G07b): 0.7 mmag, which is 1.2 times GJ 436's photon noise.

Table 1. Parameters derived from the secondary eclipse for GJ 436 b. SE stands for secondary eclipse.

Mid-SE timing [HJD]	2 454 282.333 ± 0.001
Flux decrement [ΔF_s]	0.00054 ± 0.00007
T_b at 8 μm [K]	717 ± 35
Orbital eccentricity	0.14 ± 0.01

2.2. Ground-based photometry

To assess the variability of the star, we observed GJ 436 with the Euler Swiss telescope located at La Silla Observatory (Chile) and the François-Xavier Bagnoud Observatory's (OFXB) 0.6 m telescope located at Saint-Luc (Switzerland). Observations occurred during 14 nights from May 4th to May 21th. A sequence of 10 exposures was performed every night. The same strategy used for our observation of the May 2nd transit (G07a) was applied (*V*-band filter, 80 s exposure time, defocus to ~9″). The data reduction was also similar. For our analysis of the GJ 436 variability, we also use the May 2nd out-of-transit data and the photometric lightcurves obtained with the OFXB 0.6 m telescope during our search for the transits of GJ 436 b (G07a). We scale OFXB points with Euler points because of the filters' slightly different bandpasses. At the end, our data amounts to 24 points spanning 48 days. The lightcurve is represented in Fig. 6, and discussed in Sect. 5.3.

2.3. Ground-based spectroscopy

Since the discovery of GJ 436 b (Butler et al. 2004), we obtained additional spectra of the star with the ESO HARPS spectrograph (Mayor et al. 2003). HARPS is mounted on the ESO 3.6 m telescope and is dedicated to high precision radial-velocity measurements, thanks to its resolution of 110 000 and a wavelength range coverage between 3800 and 6800 Å. To assess the stellar activity and rotation we used 23 high SNR spectra from which we measured the Ca II H+K index. Results are discussed in Sect. 5.3

3. Analysis of secondary eclipse time series

We fit a non-limb-darkened eclipse profile to the secondary eclipse data using the Mandel & Agol (2002) algorithm. The eccentricity of the orbit is considered as described in G07b, taking the values for the eccentricity e and the argument of periastron ω from M07. The formula connecting ω to the true anomaly f at the orbital location of the secondary eclipse is:

$$f = \frac{\pi}{2} + \omega. \tag{1}$$

We fix the stellar and orbital parameters to the values mentioned in G07a. The free parameters are the central epoch of the secondary eclipse T_s and the flux decrement ΔF_s. The fit procedure and the error bar estimation is similar to that described in G07b. The obtained values for T_s and ΔF_s, including their respective error bars, are given in Table 1. Figure 1 shows the best-fit theoretical curve superimposed on the lightcurve (zoomed on secondary eclipse center, binned for clarity) and the residuals of the fit.

After having derived an accurate value for the eccentricity (see Sect. 5), we perform a new fit to the secondary eclipse, taking into account the new values for the orbital eccentricity and the true anomaly at the orbital location of the eclipse, and their new error bars. The obtained values are in excellent agreement with those given in Table 1.
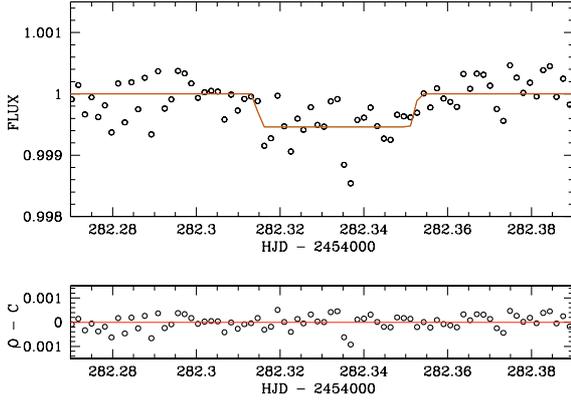
Fig. 1. *Top*: zoomed binned time series for the secondary eclipse. The best-fit theoretical curve is superimposed. Although unbinned data were used for the fit, points are binned by 5 for plotting purposes. *Bottom*: the unbinned residuals of the fit. Their rms is 0.7 mmag.
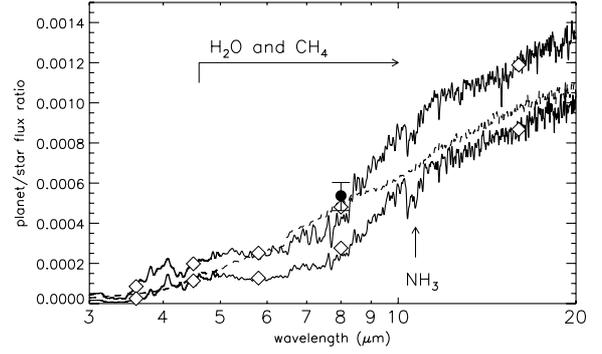

Fig. 2. Model planet-star flux ratios for GJ 436 b, assuming that the absorbed stellar flux is redistributed across the dayside only (*top curve*) and uniformly redistributed across the entire planetary atmosphere (*lower curve*). In both models, the composition is equal to that of the host star. For the wavelength range shown, the majority of the planet spectral features are produced by water, methane, and ammonia absorption. The filled black diamond is our *Spitzer* contrast measurement at 8 μm with its associated error bars, while unfilled diamonds are the model contrast values in the *Spitzer* IRAC and IRS bandpasses. The dashed line is the contrast curve for a 700 K blackbody planet spectrum.

4. Infrared radiation

While GJ 436 b is properly classified as a hot Neptune, the irradiation by the host star is weaker than for most hot Jupiters. Consequently, the contrast measurement reported here is that of the coolest exoplanet atmosphere detected so far. The atmospheric temperatures are predicted to be low enough for carbon to be bound in CH_4 (instead of CO as is the case for most hot Jupiters), placing GJ 436 b in an as yet unexplored exoplanet atmospheric regime. The temperatures should also be cool enough for NH_3 absorption to appear between 10 and 11 μm. This situation is comparable to T dwarfs, which have prominent absorption bands of NH_3 at 10.5 μm, as seen in recent *Spitzer* IRS observations (Cushing et al. 2006). In Fig. 2 we compare our 8 μm contrast measurement to synthetic planet-star flux ratios calculated following the methods described in Barman et al. (2001, 2005) for two different assumptions for the day-to-night energy redistribution. The hotter dayside model corresponds to no redistribution of energy to the night side, while the second (lower flux) model assumes very efficient redistribution of energy capable of completely homogenizing the day and night sides. As can be seen, our 8 μm measurement agrees very well with the hotter of the two models, suggesting that redistribution is fairly inefficient. However, it is impossible to constrain the bolometric flux emerging from the planet (and thus the true energy budget of the day and night sides) with a single flux measurement in one bandpass. If energy redistribution is highly depth-dependent, as indicated by recent dynamical simulations (Cooper & Showman 2005), then it remains possible that significant amounts of energy are being transported to the nightside, resulting in a warm nightside and cooler dayside at depths above or below the 8 μm photosphere. The agreement with the model spectrum suggests that observations at other *Spitzer* bandpasses should be possible, and will allow further valuable constraints on both the atmospheric composition and the energy redistribution. In particular, the 700 K blackbody planet spectrum (dashed line, Fig. 2) illustrates the value of observations at 4.5 and 16 μm as helpful probes of different atmospheric depths having different brightness temperatures. Here, we estimate a temperature of $T_b = 717 \pm 35$ K at 8 μm, by comparing the observed contrast to blackbody spectral energy distributions divided by a synthetic stellar spectrum ($T_{eff} = 3350$ K, M07), weighted by the radii ratio squared. We then varied the blackbody temperature until the 8 μm integrated contrast matched the observed contrast value.

5. Orbital analysis

5.1. The non-zero eccentricity

One noticeable characteristic of GJ 436 b is its non-zero eccentricity ($e = 0.16 \pm 0.02$ – M07). This contrasts with most known short-period exoplanets ($P < 5$ days) which have very small eccentricities, often indistinguishable from zero. Unfortunately, moderate eccentricities are difficult to constrain with radial-velocity measurements, and M07 warn that the quoted errors of the orbital parameters, based on the bootstrap technique, may lead to wrong estimates in some cases. To assess the statistical significance, they choose to use a rigorous Bayesian analysis, and find the eccentricity to be greater than 0 with a high confidence level. Nevertheless, GJ 436 b's eccentricity is only known with a large uncertainty.

To improve the determination of GJ 436 b's eccentricity we combine *Spitzer* eclipse timings with M07 radial velocities and perform a combined fit. As M07 have shown with a high confidence level, a positive radial-velocity trend is present in their data, therefore we choose a model made of a planet plus a linear drift. Our minimization is based on the Levenberg-Marquardt algorithm (Press et al. 1992) and, as a maximum likelihood approximation, minimizes the following χ^2:

$$\chi^2 = \sum_i \left(\frac{v_i - \overline{v_i}}{\epsilon_{v,i}} \right)^2 + \left(\frac{T_p - \overline{T_p}}{\epsilon_{T_p}} \right)^2 + \left(\frac{T_s - \overline{T_s}}{\epsilon_{T_s}} \right)^2, \qquad (2)$$

where v_i is the ith radial velocity given in M07, and T_p and T_s are respectively the timings of the *Spitzer* primary transit and secondary eclipse, respectively, reported in this paper. The corresponding error estimates are $\epsilon_{v,i}$, ϵ_{T_p} and ϵ_{T_s}, and $\overline{v_i}$, $\overline{T_p}$ and $\overline{T_s}$ are their corresponding computed values, according to the chosen model.

We find the χ^2 to be minimum with an orbital period $P = 2.643859$ days, a semi-amplitude $K = 18.2$ m s^{-1}, a date of the passage at periastron $T_0 = 2\,454\,198.2056714$ HJD, an argument of periastron $\omega = 350°$, an orbital eccentricity $e = 0.14 \pm 0.01$, a radial-velocity offset $\gamma = 4.2$ m s^{-1} and slope $dv/dt = 1.4$ m s^{-1} yr^{-1}.
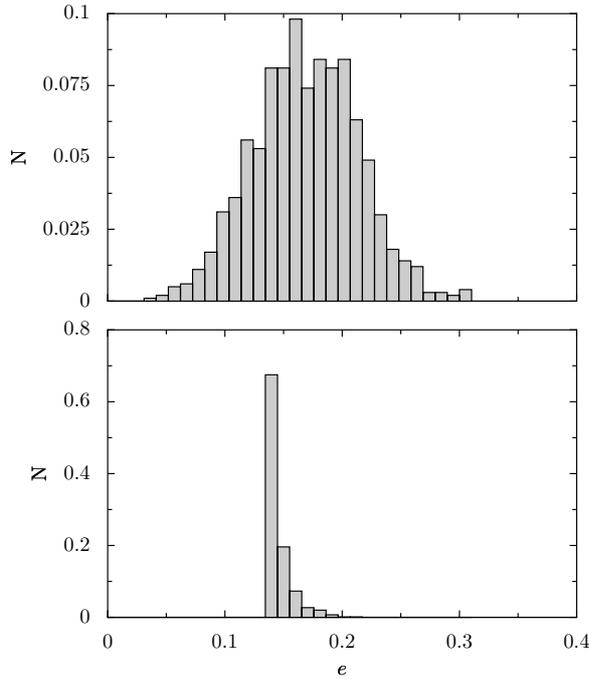
Fig. 3. Probability distributions for the eccentricity resulting from randomly generated datasets including: *Top*: radial velocity data only. *Bottom*: radial velocities + transit and secondary eclipse timings.

For this fit, the squared root of the reduced χ^2 is 1.84, marginally higher than a fit with radial velocities alone ($\sqrt{\overline{\chi}^2}|_{\text{rv only}} = 1.81$).

To derive the error of fitted orbital parameters we simulate 1000 virtual sets of new radial velocities and new eclipses timings. In each set, the radial-velocity data are randomized with a bootstrap algorithm (Press et al. 1992) and the eclipses timings are randomly generated according to a normal distribution, with mean and standard deviation given by the actual timing values and their error, respectively. Figure 3 shows these probability distributions for the eccentricity in both cases, when only the radial-velocity data are used and when a combined fit of radial-velocity and eclipses timings data is performed. The determination of eccentricity is clearly improved by the addition of both primary and secondary eclipses timings, which bring the 1-σ error on e down to 0.01.

Spitzer observations therefore strongly confirmed the unusual eccentricity of GJ 436 b. M07 pointed out that this eccentricity may be due either to its own structure (i.e. a high tidal-quality factor Q) or to an additional long-period companion periodically interacting with the planet and inducing a pumping of its eccentricity. GJ 436 b has since been captured in transit and we now have a precise measurement of its radius. Considering GJ 436 is probably more than a few billion years old, we can estimate what Q would dissipate the tidal circularization up to this age.

To match an age >2 Gyr, a $Q > 10^6$ is necessary (Adams & Laughlin 2006), which is much more than Neptune in the solar system, for which Banfield & Murray (1992) give $1.2 \times 10^4 < Q < 3.3 \times 10^5$. Thus, interaction with another companion is the most likely explanation for GJ 436 b's large eccentricity, probably due to the long-period companion suspected from the radial-velocity trend in M07 data.
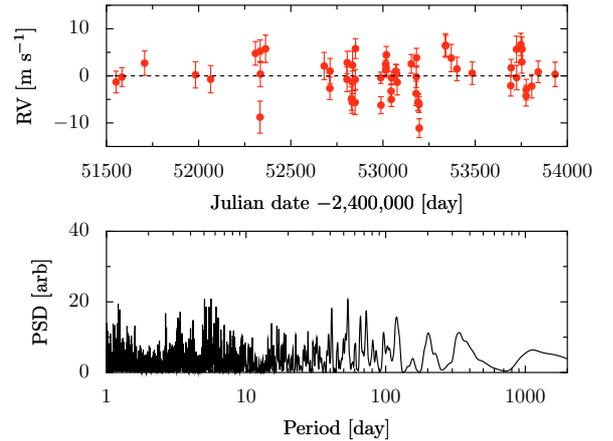

Fig. 4. Residuals around the best-fit orbital solution. *Top*: O−C with their error bars. *Bottom*: periodogram computed from residuals.

5.2. Looking for additional planets

The improvement in the determination of orbital parameters provides an opportunity to look for additional planets in the radial-velocity data. Such analysis is also motivated by the $\sqrt{\overline{\chi}}^2$ of our solution, which is larger than one.

A period analysis of the residuals around the best solution (Fig. 4) shows no significant power excess at any period. The highest peak is found at $P \sim 5.602$ days and is attributed a 92% false alarm probability by bootstrap randomizations. In conclusion, with the exception of the companion suspected in Sect. 5.1, the present data set shows no evidence for additional low mass exoplanets in the GJ 436 system.

5.3. Investigating residuals: the stellar activity

An alternative way to explain why the dispersion of the radial-velocity residuals is in excess compared to the internal errors is to invoke the stellar activity. If present on the stellar surface, spots are known to modulate the Doppler measurement and to introduce "jitter" or additional coherent signal in radial-velocity measurements (Saar & Donahue 1997).

Earlier this year we published the discovery of a $m \sin i = 11\, M_\oplus$ planet orbiting the nearby M dwarf GJ 674 (Bonfils et al. 2007). In addition to the Doppler signal induced by the planet, we clearly identified a second signal of period ~35 days in the residuals of the one-planet fit. We have shown that Ca II H&K emission lines were varying in phase with this second signal, demonstrating that it was due to a spot rather than a planet. This analysis was given further credit by a clear photometric counterpart to the spectral-index variation.

To investigate the activity of GJ 436, we can thus apply the same spectroscopic diagnostic as we did for GJ 674, thanks to Harps spectra we have been obtaining since 2004. Figure 5 represents the periodogram of Ca II H+K index measured on 23 high SNR spectra of GJ 436. It displays a power excess around $P \sim 48$ days that identifies the rotation period of GJ 436. Bootstrap randomizations give a false alarm probability <1% for this peak.

Moreover, complementary photometric observations we performed to monitor the long-term activity of GJ 436 (Fig. 6) confirm that a spot is present on the surface of GJ 436 and that the rotational period is likely to be more than 40 days. On a 50-day time span, the variation of the flux has an amplitude of ~1%. We know from the spectral index variation that 50 days is close
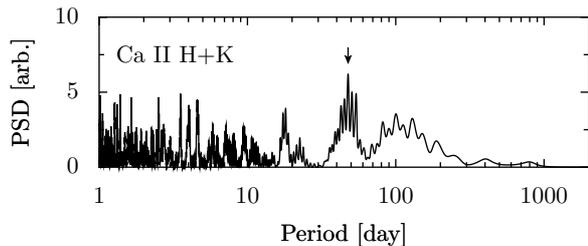
Fig. 5. Ca II H+K periodogram obtained from high SNR spectra with Harps spectrograph. The arrow points at the power excess around $P \sim$ 48 days.
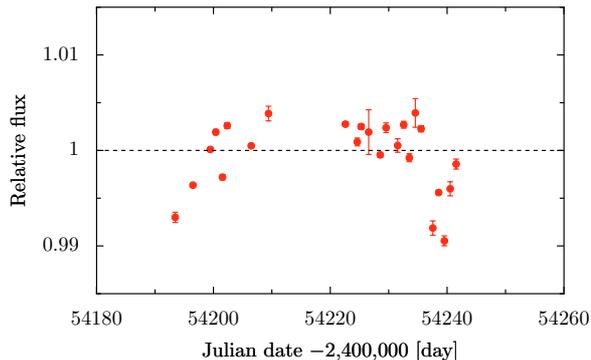

Fig. 6. Long-term lightcurve obtained with the Euler 1.2 m telescope at ESO La Silla Observatory and the 0.6 m telescope at FXB Observatory.

to the rotational period, and it is thus reasonable to assume this amplitude for the photometric signal. With an estimate of the amplitude of the photometric variation, plus an approximate rotational period, it becomes possible to estimate the amplitude of the activity induced radial-velocity variation.

Saar & Donahue (1997) have done some simulations and found that the radial-velocity amplitude K_s induced by a spot follows approximately the relation:

$$K_s[\text{m s}^{-1}] \sim 6.5 \times f_s^{0.9} \times v \sin i, \tag{3}$$

where f_s is the size of the spot (expressed in percent of the stellar disk) and $v \sin i$ is the projected rotational velocity of the star.

In the case of GJ 674, considering its radius ($0.34\,R_\odot$) and its rotational period (34.8 days), we calculate a $v \sin i$ of $0.5\,\text{km s}^{-1}$. Equation (3) then converts the observed flux variation ($\sim 2.6\%$) into a radial-velocity amplitude $K_s \sim 8\,\text{m s}^{-1}$, close to the measured amplitude ($6\,\text{m s}^{-1}$).

The same numerical application for GJ 436, with a radius $R_\star = 0.463\,R_\odot$ (G07b), a rotational period $P_{\text{rot}} \sim 45$ days, and a filling factor $f_s \sim 1\%$, leads to $K_s \sim 3\,\text{m s}^{-1}$. The spot is thus responsible for a typical dispersion of $\sim 2\,\text{m s}^{-1}$, which, when combined with the typical radial-velocity errors ($\sim 2.4\,\text{m s}^{-1}$), explains most (if not all) of the dispersion observed for the residuals around our best solution ($\sim 4\,\text{m s}^{-1}$). Ultimately, to better weight the errors between radial-velocity data and eclipses timings data, we introduce this "jitter" in our fitting procedure. Its impact is negligible, as the estimated parameters remain unchanged.

6. Conclusions

Since its discovery, GJ 436 b has been shown to be a peculiar planet and has raised a lot of interest from the community regarding its composition, or the presence of supplementary planets in the system. *Spitzer* data gathered from the primary and

secondary eclipse are of great help in answering some of those questions as discussed in G07b and in this present study.

We learn from the infrared emission measurements at 8 μm and planetary atmospheres models that GJ 436 b is characterized by an envelope composed of H, He, H_2O and CH_4. Also, our contrast measurement is consistent with a model planet that has very inefficient day-to-night redistribution at 8 μm photospheric depths on the dayside.

Moreover, transit and secondary eclipses timings combined with radial velocities prove that GJ 436 b has an eccentricity significantly greater than zero. Considering a reasonable tidal dissipative factor, we estimated the orbital circularization timescale to be probably shorter than the age of GJ 436. We therefore conclude that the non-zero eccentricity is probably the result of a dynamical interaction with an additional companion in the system, maybe the long-period companion suspected from the radial-velocity trend in M07 data.

In the course of our orbital analysis we try to find an additional planet around GJ 436, but no significant periodicity is found in the residuals of our best fit. Conversely, we identify that GJ 436 has a spotted surface and probably rotates with a period $P_{\text{rot}} \sim 48$ days. We estimate that this magnetic activity adds noise to the radial-velocity signal at a level of $\sim 2\,\text{m s}^{-1}$, therefore explaining most (if not all) of the residual dispersion around our best solution.

Nevertheless, the full potential of *Spitzer* concerning GJ 436 b has not been explored yet, especially regarding thermal emission spectral coverage. Complementary observations in the 3.6, 4.5, 5.8-μm IRAC, 16-μm IRS and 24-μm MIPS channels are due between November 2007 and February 2008. They will certainly bring new constraints on the atmosphere composition of this planet.

References

Adams, F. C., & Laughlin, G. 2006, ApJ, 649, 1004
Banfield, D., & Murray, N. 1992, Icarus, 99, 390
Barman, T. S., Hauschildt, P. H., & Allard, F. 2001, ApJ, 556, 885
Barman, T. S., Hauschildt, P. H., & Allard, F. 2005, ApJ, 632, 1132
Bonfils, X., Mayor, M., Delfosse, X., et al. 2007, A&A, 474, 293
Butler, R. P., Vogt, S. S., Marcy, G. W., et al. 2004, ApJ, 617, 580
Cooper, C. S., & Showman, A. P. 2005, ApJ, 629, L45
Cushing, M. C., Roellig, T. L., Marley, M. S., et al. 2006, ApJ, 648, 614
Deming, D., Harrington, J., Laughlin, G., et al. 2007, ArXiv e-prints, 707
Fazio, G. G., Hora, J. L., Allen, L. E., et al. 2004, ApJS, 154, 10
Gillon, M., Pont, F., Demory, B.-O., et al. 2007a, A&A, 472, L13
Gillon, M., Demory, B.-O., Barman, T., et al. 2007b, A&A, 471, L51
Giorgini, J. D., Yeomans, D. K., Chamberlin, A. B., et al. 1996, in BAAS, 28, 1158
Houck, J. R., Roellig, T. L., van Cleve, J., et al. 2004, ApJS, 154, 18
Mandel, K., & Agol, E. 2002, ApJ, 580, L171
Maness, H. L., Marcy, G. W., Ford, E. B., et al. 2007, PASP, 119, 90
Mayor, M., Pepe, F., Queloz, D., et al. 2003, The Messenger, 114, 20
Press, W. H., Teukolsky, S. A., Vetterling, W. T., & Flannery, B. P. 1992, Numerical recipes in FORTRAN. The art of scientific computing (Cambridge: University Press), 2nd edn.
Rieke, G. H., Young, E. T., Engelbracht, C. W., et al. 2004, ApJS, 154, 25
Saar, S. H., & Donahue, R. A. 1997, ApJ, 485, 319